AI-guided discovery of a novel ATP/ADP binding domain in plant HAK transporters that regulates K^+/Na^+ homeostasis

Fan Yang[1,*], Qinrui Wang[2,*], Junzhao Yang[1], Ruoxian Xia[1], Yaming Lu[1], Xia Xu[1], Peng Fu[1], Jiaqi Zhou[1], Yutian Jia[1], Han Wen[3,4,5,6], and Guanghui Yang[1,7,8]

[1]Frontiers Science Center for Molecular Design Breeding, State Key Laboratory of Plant Environmental Resilience, College of Biological Sciences, China Agricultural University, Beijing 100193, China

[2]DP technology, Beijing 100190, China

[3]Beijing Advanced Center of RNA Biology (BEACON), Peking University, Beijing, 100871, China.

[4]Institute for Advanced Algorithms Research, Shanghai, 201799, China.

[5]AI for Science Institute, Beijing, 100085, China.

[6]State Key Laboratory of Medical Proteomics, China

[7]School of Interdisciplinary Life Sciences, China Agricultural University, Beijing 100193, China

[8]Lead contact

*These authors contribute equally in this study.

To whom correspondence should be addressed. E-mail: guanghuiyang@cau.edu.cn

Abstract

Maintaining Na^+/K^+ homeostasis is fundamental for plant environmental adaptation. Using domain classification of plant Na^+/K^+ transport proteins, and AI-based ligand screening integrated with biochemical characterization, we identified a previously unannotated cytoplasmic domain (CPD) in plant HAKs as a novel ATP/ADP-binding fold. We demonstrate that ATP/ADP binding to the CPD directly couples to the gating of ion transport, a regulatory mechanism previously unknown in this transporter family. Cryo-EM structures of *Arabidopsis* HAK5 in ADP-bound and ligand-free states, alongside *Zea mays* HAK4 in an ATP-bound state, revealing a distinctive autoinhibitory mechanism. In the ADP-bound state, the CPD physically obstructs the transmembrane ion pathway. Conversely, the gain-of-function mutant *At*HAK5$_{D152A}$ triggers a downward translocation of the CPD to release this inhibition, which is corroborated by the ATP binding conformation of *Zm*HAK4. Our study defines the structural basis for ATP/ADP-associated gating in plant HAK transporters, providing a novel molecular framework for engineering salt-tolerant crops.

INTRODUCTION

Maintaining Na^+/K^+ homeostasis is a cornerstone of plant survival, particularly under abiotic stresses such as salinity and potassium deficiency[1]. These two ions play antagonistic roles in plant physiology: whereas K^+ is an essential macronutrient vital for enzymatic activation, osmotic regulation, and membrane potential stabilization, excessive Na^+ accumulation is cytotoxic, disrupting cellular functions and ionic balance[2-7]. Consequently, plants have evolved sophisticated regulatory networks to maintain an optimal Na^+/K^+ ratio, a process central to environmental adaptation[3; 6; 8-12].

This ionic equilibrium is orchestrated by a diverse array of membrane transport proteins, including Shaker-type K^+ channels[11; 12], HKT transporters[13], sodium/hydrogen exchangers[14; 15], the HAK/KT/KUP family[16], and some cyclic nucleotide-gated ion channels (CNGCs)[17; 18]. To systematically explore the functional landscape of plant Na^+/K^+ transport proteins, we performed a comprehensive domain-clustering analysis across multiple transport protein families using TED/CATH databases[19; 20], UniProt annotations[21], and structural models (Figure 1A). A defining feature of most plant ion transporters and channels—with the notable exception of the HKT family—is the presence of a regulatory cytoplasmic domain (CPD)[22-24]. While the functions of these CPDs remained elusive for decades, recent structural breakthroughs have begun to unveil their roles in modulating transporter or channel activity. For instance, the CPDs of AKT1 and SOS1 mediate autoinhibition-activation transitions, while those in plant CNGCs harbor an intrinsic ligand-binding modules [25-30]. Although plant HKTs lack a CPD, their prokaryotic homologs (e.g., KtrAB and TrkAH) utilize RCK (Regulate conductance of K^+) domains that bind ATP or ADP to regulate ion transport [31-34]. This pipeline identified a conserved

C-terminal CPD in the HAK family that lacked any functional annotation. Intriguingly, FoldSeek[35]- and Dali[36]-based structural alignment revealed no characterized homologs, suggesting that this CPD represents a novel structural fold (Figure 1A; Figure S1). The HAK family members play pivotal roles in high-affinity K^+ uptake, long-distance translocation, and Na^+ retrieval[16]. Elucidating the molecular basis of HAK regulation is not only a fundamental biological question but also essential for engineering stress-resilient crops. Thus, this discovery raises a compelling question: do plant HAKs utilize their CPDs to regulate their function?

In this study, by employing Boltz2-based ligand screening and biochemical characterization[37], we demonstrate that the unannotated domain of HAK family constitutes a novel structural fold with ATP/ADP-binding capacity—a regulatory feature that has remained entirely unrecognized across all previous studies. Through cryo-EM analysis of *Arabidopsis* HAK5 (*At*HAK5) and *Zea mays* HAK4 (*Zm*HAK4), we provide the first structural evidence of ATP/ADP-binding pockets in plant HAKs. Our data reveal a distinctive autoinhibitory mechanism where the CPD physically obstructs the ion pathway in an ADP-bound state, a conformation that is released upon ATP binding or specific gain-of-function mutations. These findings establish a new paradigm for the ATP/ADP-associated regulation of plant Na^+/K^+ homeostasis.

RESULTS

Discovery of a novel ATP/ADP-binding fold in the HAK Family

Given that the CPD of the HAK family lacked any functional annotation, we sought to identify its potential role using state-of-the-art structural alignment tools. We focused on

*At*HAK5, the most characterized member of this family[38; 39]. Using the AlphaFold3[40]-predicted *At*HAK5 CPD as a query, a FoldSeek search [35]returned only other HAK family members, highlighting the domain's high conservation while underscoring its uniqueness. Notably, The Encyclopedia of Domains (TED[19]) failed to assign it to any known CATH[20](Class, Architecture, Topology, and Homologous superfamily) classification (Figure S1A). A subsequent Dali search[36] identified a universal stress protein from *Haemophilus influenzae* (PDB: 1JMV) as the top hit[41]. These two domains exhibit divergent topology and share only 8% sequence identity with a significant root-mean-square deviation (RMSD) of 3.1 Å (Figure S1B-D). Collectively, these findings suggest that the HAK CPD represents a previously uncharacterized structural fold.

Structural analysis of the *At*HAK5 CPD revealed a prominent, positively charged pocket, suggesting a capacity for binding anionic ligands (Figure 1B). Although *At*HAK5 shares only 19.37% sequence identity with its prokaryotic ortholog *Bacillus subtilis Bs*KimA—which binds the bacterial second messenger c-di-AMP—and possesses a distinct fold, we hypothesized that the plant HAK CPD might have evolved to bind plant nucleotides derivatives[42]. To test this systematically, we performed AI-aided ligand docking across 430 HAK homologs from various crop species against seven candidate ligands, including prokaryotic c-di-AMP, four cyclic monophosphate nucleotides (cNMPs), and the primary cellular energy carriers, ATP and ADP (Figure 1C). From 15,050 generated models, we utilized the interface predicted template modeling (ipTM) score to evaluate binding confidence, applying a stringent criterion of ipTM > 0.8 to identify high-confidence predictions. While plant second messengers like 3′5′-cAMP or 2′3′-cAMP failed to meet this threshold, ATP and ADP emerged as the only ligands consistently

yielding ipTM scores exceeding 0.8, exhibiting superior structural complementarity and pLDDT scores (Figure 1C).

To validate these predictions, we performed surface plasmon resonance (SPR) using purified full-length *At*HAK5 (Figure S2). Consistent with the *in silico* models, *At*HAK5 exhibited high-affinity binding to both ATP and ADP, with dissociation constants (K_D) of approximately 50 nM and 66 nM, respectively (Figure 2). To determine the functional consequences of this binding, we employed a two-electrode voltage clamp (TEVC) assay in *Xenopus* oocytes[43]. While ADP injection had no significant effect on K^+ currents, ATP injection triggered a substantial increase in *At*HAK5-mediated K^+ conductance (Figure 2). Together, these results demonstrate that the *At*HAK5 CPD is a functional ATP/ADP-binding module, where the ATP/ADP potentially acts as a switch to gate K^+ transport—a regulatory mechanism previously unknown in this transporter family.

Coordination of ADP is accompanied with an autoinhibitory conformation of *At*HAK5

Albeit AlphaFold3[40] and Boltz2 [37]provided high-confidence models for ligand binding in *At*HAK5, the predicted structures for the ATP-bound and ADP-bound states remained nearly identical, which is insufficient to provide a structural rationale for their different effects on electrophysiological activity. To uncover the conformational dynamics and the authentic binding modes of endogenous ligands that AI might overlook, we determined the cryo-EM structure of the *At*HAK5 homodimer at an overall resolution of 3.04 Å. Each *At*HAK5 protomer consists of a 12-helix N-terminal transmembrane domain (TMD) and a C-terminal CPD, interconnected by a cytosolic bridge helix. Unlike the domain-swapped

architecture observed in its bacterial ortholog *Bs*KimA, the dimerization of *At*HAK5 is driven exclusively by CPD-CPD interactions (Figure 3; Figure S3; Figure S4; Table S1), suggesting a distinct evolutionary regulatory trajectory for the plant HAK family.

Intriguingly, prominent non-protein densities were observed within each CPD, which fitted well as ADP (Figure 3A). Such ADP molecules must be endogenously bind to the CPD as no exogenous ligands were supplemented during purification. Mass spectrometry (MS) definitively identified this endogenous ligand as ADP (Figure 3B), confirming that *At*HAK5 captures cellular ADP with high affinity and validating our initial *in silico* screening hypothesis with high fidelity. The ADP molecule is meticulously anchored within the pocket: the adenine and ribose moieties form hydrogen bonds with Ile593, Glu565 and Gly733 while the diphosphate group is stabilized by hydrogen bonds with His527, Thr735 and Tyr755, accompanying with a dense salt-bridge network involving Arg406 and Lys759 (Figure 3C-D). The relative conservation of these residues across the HAK family suggests that this ATP/ADP-binding capability maybe a universal attribute of plant Na^+/K^+ homeostasis allowing variation to support member-specific regulation (Figure S5).

To integrate these structural findings with transport function, we performed alanine scanning on the ADP-coordinating residues and assessed their activity in the K^+-deficient yeast strain R5421. Notably, while the E565A and Y755A mutations slightly impaired K^+ transport, the T735A and K759A variants resulted in a gain-of-function phenotype (Figure 3E). These divergent functional responses indicate that the CPD does not merely bind ADP but acts as a regulatory tuner, where the specific coordination of the ADP is coupled with the changes of the transport activity.

The K^+ transport pathway within the TMD of each *At*HAK5 protomer was enclosed by TM1, TM3, TM6, and TM8 (Figure 4A). Residues Asp72, Thr75 and Tyr79 from TM1 and Tyr450 from TM10 generate a negatively charged cavity where K^+ is captured (Figure 4B). Within this cavity, Asp72 may facilitate the K^+ coordination, while Tyr79 likely functions as an external gate to occlude the bound substrate, a mechanism structurally analogous to the equivalent residues in *Bs*KimA[44]. Consistent with their roles in substrate coordination and gating, mutations D72A and Y79A abolish transport, while T75A and Y450A subtly enhance K^+ uptake by altering the hydrogen bond networks (Figure 4B, D)

The K^+ transport pathway extends into the CPD and at the end of pathway, residue Asp123 from the intracellular loop connecting TM2 and TM3 and residue Tyr628 from CPD both insert into the pathway and form a hydrogen-bond interaction, which may obstruct K^+ transport efficiency (Figure 4A, C; Figure S6). Disrupting this interaction by single mutants Y628A and D123A exhibit enhanced K^+ transport activity (Figure 4D). Furthermore, the network of hydrogen bonds (e.g., Arg400-Thr595) and salt bridges (e.g., Asp152–Lys594 and Glu417–Arg600) further stabilizes this TMD–CPD interface. Systematic alanine scanning of these interfacial residues revealed that while none markedly impaired function, several variants (particularly D152A and K594A) exhibited profoundly enhanced K^+ transport. Collectively, these structural and functional data indicate that in the ADP-bound state, the CPD inserts into the TMD to form a physical barrier. This TMD–CPD interface acts as an autoinhibitory gate. Disrupting this interface effectively release the transporter from its inhibited state.

The *At*HAK5 activation is coupled to ADP release and CPD rearrangement

To observe the ATP binding and regulating mode of *At*HAK5, we attempted to capture an ATP-bound conformation of *At*HAK5 by supplementing 5 mM ATP throughout the whole protein purification and cryo-EM sample preparation process. However, the resulting structure remained in an ADP-bound autoinhibited state. This suggests that the ADP-bound form represents a highly stable energetic ground state, potentially masking the ATP-induced transition under *in vitro* conditions. To circumvent this stability, we focused on the D152A variant, which resides at the TMD-CPD interface and exhibited the most substantial gain-of-function phenotype in yeast growth assays. We determined the cryo-EM structure of *At*HAK5$_{D152A}$ at 3.46 Å resolution (Figure 4E; Figure S7). Remarkably, the *At*HAK5$_{D152A}$ density map revealed a ligand-free pocket, and mass spectrometry confirmed that this point mutation was sufficient to trigger the complete release of ADP (Figure 4E).

Structural comparison revealed that this mutation-induced ADP release facilitates a massive conformational reorganization (RMSD = 2.974 Å, 8915 to 8915 atoms). The CPD undergoes a pronounced downward translocation, moving away from the TMD and completely disengaging from the pore exit (Figure 4E and Figure S6). This shift increases the distance between Asp123 and Tyr628 to 13.2 Å, effectively dismantling the autoinhibitory barrier. These results demonstrate that disrupting the specific TMD-CPD interface—either by mutation or potentially by physiological ATP binding—is the key event that triggers ADP dissociation and the physical release of the autoinhibitory plug. This unlocked conformation provides a structural template for the activated state of the HAK family.

The ATP-bound structure of *Zm*HAK4 reveals a conserved mechanism for

autoinhibition release

To determine whether the structural principles observed in *At*HAK5 are conserved across the HAK family, we investigated *Zm*HAK4, a maize ortholog recently identified as a Na^+-selective transporter, representing the third class of Na^+-selective transporters that confer salt tolerance[45]. We employed a similar purification strategy and determined the cryo-EM structure of *Zm*HAK4 at an overall resolution of 3.13 Å (Figure S8). In striking contrast to the wild-type (WT) *At*HAK5, the CPD of *Zm*HAK4 contained clear non-protein density corresponding to ATP rather than ADP (Figure 5A). In this binding pocket, residues Asn532, Leu562 and Gly651 anchor the adenine and ribose moieties through hydrogen bonds. The triphosphate group is coordinated by a network of hydrogen bonds and salt bridges with Ser681, Arg373, Arg494, Lys652, and His676 (Figure 5B). Compared to the ADP-bound pocket of *At*HAK5, the ATP-binding site in *Zm*HAK4 undergoes a spatial displacement resulting from a downward shift of the CPD, causing the γ-phosphate of ATP to bend toward the adenosine moiety (Figure 5B, C).

Structural comparisons reveal that the ATP-bound conformation of *Zm*HAK4 closely recapitulates the autoinhibition-released state of *At*HAK5$_{D152A}$ (Figure 5D, E). First, the *Zm*HAK4 CPD is physically displaced from the TMD. Specifically, Tyr595 (equivalent residue to *At*HAK5 Tyr628) exhibits a 13.6 Å displacement from Asp87 (equivalent residue to *At*HAK5 Asp123), leaving the transport path unlocked (Figure 5D-F). Additionally, an upward movement of the intracellular helix linked to TM3—also observed in the activated *At*HAK5 mutant—likely destabilizes the TMD-CPD interface, providing the CPD with the mobility required for activation.

To reconcile why ATP binds stably to *Zm*HAK4 but not to the activated *At*HAK5$_{D152A}$,

we characterized the binding environment of the ATP/ADP pocket. This divergence might be rooted in the electrostatic properties of the binding pocket. In *Zm*HAK4, the neutral Asn532 coordinates the adenosine head, whereas in *At*HAK5, this position is occupied by the negatively charged Glu565. This acidic residue likely generates electrostatic repulsion with the highly charged triphosphate group of ATP, rendering the ATP-bound state unstable in *At*HAK5 (Figure 5G). To corroborate this assumption, we swapped the Glu565 in *At*HAK5 to asparagine in *Zm*HAK4. The *At*HAK5$_{E565N}$ exhibited enhanced transport activity, confirming that the ATP-bound architecture of *Zm*HAK4 represents a common activated template for the HAK family (Figure 5H).

DISCUSSION

In this study, by using an AI-guided pipeline, we identify the CPD of plant HAK family is a previously uncharacterized ATP/ADP-binding module. By integrating electrophysiological validation with structural dynamics, we demonstrate that *At*HAK5 is maintained in an autoinhibited state by endogenous ADP. Although an ATP-bound structure of *At*HAK5 remained undetermined due to an intrinsic energetic barrier and electrostatic repulsion (Glu565), our biophysical and functional data confirm that ATP binding triggers a transient but robust activation of K^+ currents. The discovery of the *At*HAK5 gain-of-function mutant—and its structural homology to the ATP-bound *Zm*HAK4—provides a bridge between the locked and unlocked states. Such observations support a dynamic plug-and-release activation mechanism of HAK family, where the CPD physically obstructs or reveals the ion pore in response to cellular adenylate status (Figure 6). The regulatory mode proposed here distinguishes the HAK family from other well-characterized plant

transporters. While the activity of proteins like AKT1, CNGCs, and SOS1 is primarily modulated by auxiliary subunits or the flexibility of their regulatory domains, HAK transporters represent a novel category of regulation governed by direct ligand binding within a highly specialized fold[25-30]. It is topologically divergent from the conserved TeaD-like scaffolds of human cation-chloride cotransporters (CCCs) and bacterial KtrA/TrkA subunits, as well as the structural found in CLC channels[31; 33; 46-51]. This structural novelty suggests that plants evolved a unique protein architecture to couple the ATP/ADP exchange directly to transmembrane K^+/Na^+ fluxes.

This mode offers a strategic advantage for plant survival. *At*HAK5, which functions under extreme K^+ deficiency, is strictly regulated to prevent ion leakage, as evidenced by its high-affinity binding to ADP and the resulting autoinhibited conformation. In contrast, *Zm*HAK4, which plays a critical role in salinity response in maize, appears energetically optimized for ATP-bound activation to prevent Na^+ overground translocation[45]. Considering the physiological role of different HAK family members, how the level of ATP and ADP in different tissues of plant varies under stress are worth future research. The discovery that a single-point variation (Glu565 in *At*HAK5 vs. Asn532 in *Zm*HAK4) can reshape the energetic landscape of the binding pocket highlights the precision of this evolutionary tuning. Furthermore, our findings provide a structural rationale for previous autoinhibition hypothesis: the segment (residues 571–633) indeed forms the physical plug against the TMD, while the downstream region acts as the ATP/ADP binding module[52].

Finally, our work opens new avenues for exploring the mechanistic crosstalk between ATP/ADP exchange and post-translational modifications in fine-tuning the activity of the HAK family. Phosphorylating the N-terminal of *At*HAK5 by the kinase complex

CIPK23/CBL1 was reported to release autoinhibition state[52; 53]. Whether phosphorylation activates the transporter by driving a comparable conformational switch? The AlphaFold3 [40]modeling suggests that phosphorylation by the CIPK23/CBL1 complex may induce a conformational switch superimposable onto the *At*HAK5$_{D152A}$ structure (Figure S9). This implies that phosphorylation and ATP binding may act synergistically—where phosphorylation lowers the energetic barrier for CPD displacement, thereby priming the transporter for ATP-mediated activation. Given the high conservation of these structural motifs across major crops, these insights provide a foundational framework for understanding plant resilience and offer precise molecular targets for breeding stress-resistant varieties in the future.

METHODS

Protein–Ligand Complex Structure Prediction

A curated set of HAK transporters were selected for this study. For each target protein, complex structures were generated with a panel of nucleotide and cyclic nucleotide ligands, including 2',3'-cAMP, 2',3'-cGMP, 3',5'-cAMP, 3',5'-cGMP, ADP, ATP, and di-cAMP. Protein–ligand complex structure prediction was performed using Boltz2[37], a deep learning–based framework for multimer and protein–small molecule complex modeling. For each protein–ligand pair, five independent structure predictions were generated using the Boltz2 diffusion-based sampling procedure, enabled with the options --use_msa_server and --diffusion_samples 5[37]. This strategy was adopted to account for stochastic variability in the diffusion process and to explore alternative ligand binding poses. This criterion ensured that the selected complex exhibited the most confident and well-defined

295 protein–ligand interaction geometry according to the Boltz2 confidence metrics[37].

296

297 **Two-electrode voltage Clamping**

298 *At*HAK5 cDNA was cloned into the pGEM-HE vector. In vitro Transcription and
299 capped RNAs (cRNAs) were synthesized from linearized plasmid DNA template using the
300 T7 High Yield RNA Transcrip tion Kit and Vaccinia Capping Enzyme Kit (Vazyme),
301 according to the manufacturer's recommendations. The quality of the cRNA was checked
302 by quick agarose gel electrophoresis. Stage V-VI oocytes were obtained from *Xenopus*
303 *laevis* and defolliculated using 2 mg/ml collagenase and trypsin inhibitor for a duration of
304 2 hours. 10ng cRNA in 30nL was injected into the treated oocytes, control oocytes were
305 injected of 30 nL RNA-free water. The injected oocytes were cultured at a temperature of
306 18 °C for 2 days in ND-96 buffer (containing 2 mM KCl, 96 mM NaCl, 1 mM $MgCl_2$, 1.8
307 mM $CaCl_2$, 5 mM HEPES pH 7.5, and 0.1g/ml gentamycin). Oocytes were voltage-
308 clamped using a Axoclamp 900A amplifier (Axon Instruments) and monitored by computer
309 through Digidata 1440A converter (Axon CNS) and Clampex 11.2 software (Axon
310 Instruments). The pipette solution contained 3 M KCl. The standard bath solution contained
311 1 mM $CaCl_2$, 2 mM KCl, 1 mM $MgCl_2$, 0.1 mM $LaCL_3$ and 10 mM MES/Tris (pH 5.5),
312 the osmolality was adjusted to 220 mOsmol kg^{-1} by 1M mannitol. Voltage steps were
313 applied from +40 to –200 mV in –20mV decrements during 1.0 s, from a holding potential
314 of –60mV. Each step begins with 0.23 s and ends with 0.37 s at the resting potential of the
315 oocyte membrane in the bath solution. For recording of *At*HAK5 with test ligands, 25 nL
316 of 5 mM ATP or ADP was separately injected into oocytes that have injected of *At*HAK5
317 cRNA or RNA-free water 2 days ago. ATP and ADP injected oocytes were recorded

immediately. Statistical analysis was performed using Clampfit 10.7 and GraphPad Prism 7.

Purification of *Arabidopsis thaliana* HAK5 and *Zea maize* HAK4

The cDNA of Arabidopsis thaliana *At*HAK5, *At*HAK5$_{D152A}$ and *Zm*HAK4 was subcloned into the pFastBac1 (Invitrogen) vector with a N-terminal FLAG tag (DYKDDDK), respectively. *At*HAK5$_{D152A}$ was induced by a two-step PCR. The recombinant proteins were expressed using the Bac-to-bac system following the manufacturer's (Invitrogen) protocol. Briefly, bacmids of targets were extracted from DH10Bac cell and P2 baculovirus was used to infect Sf9 insect cell with 30 mL P2 baculovirus added into 1L Sf9 cells at a density of ~3.0 × 10^6 cells mL^{-1}. *At*HAK5, *At*HAK5$_{D152A}$ and *Zm*HAK4 were overexpressed in Sf9 insect cells grown in the Serum-Free Medium (YSK BIO) for 60 h in 110 rpm, 27℃. Cells were collected and homogenized in the buffer containing 25 mM HEPES (pH 7.4) and 150 mM KCl (for *At*HAK5 and *At*HAK5$_{D152A}$) or 150 mM NaCl (for *Zm*HAK4) supplemented with protease inhibitor cocktails containing 1 mM phenylmethylsulfonyl fluoride, 1.3 μg/mL aprotinin, 0.7 $\mu g/mL^{-1}$ pepstatin and 5 μg/mL leupeptin. The suspension was supplemented with lauryl maltose neopentyl glycol (LMNG, Anatrace) to a final concentration of 1% (w/v) and cholesteryl hemisuccinate tris salt (CHS, Anatrace) to 0.1% (w/v). After incubation at 4 °C for 2 h, the mixture was centrifuged at 200,000 × g for 30 min, then the supernatant was applied to 1 mL anti-Flag M2 affinity gel (Sigma) by incubating at 4 °C for 1h. The resin was rinsed three times using wash buffer: 25 mM HEPES (pH 7.4), 150 mM KCl or NaCl, 0.02% GDN. Then the target protein was eluted with wash buffer plus 200 μg/ml flag peptide. The eluted protein was concentrated

using a 50-kDa cut-off Centricon (Millipore) and subsequently applied to Superose-6 increase column (GE Healthcare) in the buffer containing 25 mM HEPES (pH 7.4), 150 mM KCl or NaCl and 0.006% GDN. The peak fractions were collected and concentrated to ~5 mg/mL for cryo-EM analysis. For purification of *At*HAK5 added with ATP, 0.1 M ATP stock was supplemented into the collected cells to a finally concentration of 5 mM and all buffers used are the same as that of *At*HAK5 except for 5 mM ATP adding.

Cryo-EM sample preparation, data collection and processing

Quantifoil 300 mesh R1.2/1.3 Au grids were glow discharged for 35s at medium radio frequency level of Plasma Cleaner PDC-32G (Harrick). Aliquots of 4 μL proteins were applied onto glow-discharged holey carbon grids. The grids were blotted for 3.5 seconds at 8 ℃ under 100% humidity and flash-frozen in liquid ethane using Vitrobot Mark IV (Thermo Fisher Scientific). The grids were stocked in liquid nitrogen and first screened on 200kV Tecnai Arctica microscope, grids with high quality were further used for data collection. High-resolution cryo-EM images were collected using a 300 kV Titan Krios transmission electron microscope (TEM) equipped with a Gatan K3 Summit direct electron detector and a GIF Quantum energy filter (slit width 20 eV, Gatan) operating in super-resolution counting mode. Defocus values ranging from −1.3 to −1.8 μm were applied throughout the data acquisition process. Each micrograph was dose-fractionated into 32 frames with a cumulative electron dose of ~50 $e^{-}\cdot Å^{-2}$ and a total exposure time of 2.56 s. Data collection was fully automated and controlled using EPU software (Thermo Fisher Scientific).

Model building and structure refinement

The initial models for *At*HAK5, *At*HAK5$_{D152A}$ and *Zm*HAK4, based on predictions from AlphaFold3[40] or Boltz2[37], were employed as foundations for fitting the cryo-EM density. Subsequent manual refinement of the atomic model was conducted using COOT[54]. Following these, structural optimization in real space were achieved using PHENIX[55], incorporating secondary structure and geometric restraints. PyMOL[56](open source) and UCSF ChimeraX[57] were used to analyze cryo-EM maps and structures and prepare figures.

Yeast strains and growth experiments

The *Saccharomyces cerevisiae* 9.3 yeast strain (MATa, ena1Δ::HIS3::ena4Δ, leu2, ura3-1, trp1-1, ade2-1, trk1Δ, trk2::pCK64) was used for *At*HAK5 and mutant derivatives growth experiments[58]. The different constructs were cloned into p415GPD vector through a two-step PCR, plasmids were transformed into yeast following a standard protocol and then screened on solid SD media plates at 28℃ for 3 d. For growth tests, overnight cultures were brought to OD_{600}=1.0 and then 3-5 μL drops of decimal dilutions of the cell suspensions were spotted onto solid AP media plates. Plates were incubated at 28°C for 3–4 d.

ACKNOWLEDGMENTS

We thank the Cryo-EM Facility at Tsinghua University, Peking University, and Shuimu BioSciences for the support in cryo-EM data collection. We thank Lina Xu and Yusong Wang in Metabolomics Facility at Technology Center for China National Protein Sciences, Tsinghua University, for small molecule ligand MS analysis. We thank Zi Yang at

Biological Sample Preparation and Identification Platform, Tsinghua University, for SPR analysis. We thank Professor Yan Guo and Professor Yi Wang for the thoughtful suggestions on the functional studies.

FUNDING

This work was supported by the National Key R&D Program of China (2022YFA1303400); National Natural Science Foundation of China (32422038 to G.Y.); Chinese Universities Scientific Fund (2025TC135; 2024TC032; 31051301; 00114332 to G.Y.); China Agricultural University Young Talent Program in Life Science (Grant No. 008 to G.Y.), Pinduoduo-China Agricultural University Research Fund (Grant No. PC2023B01010 to G.Y.); Cangzhou Special Science and Technology Project for Drought-Alkali Tolerant Wheat Industry (20241001006N). Q.W. is Sponsored by Beijing Nova Program.

AUTHOR CONTRIBUTIONS

G.Y. initiated the supervised the project. G.Y. and F.Y. analyzed the sequence and structural clustering. F.Y. prepared the sequences. Q.W. and H.W. preformed Boltz2 based prediction. F.Y. and Y.L. prepared the protein sample. F.Y. performed the electrophysiological experiments. F.Y. and R.X. performed the yeast growth experiments. F.Y., X.X. and J.Y. collected the EM data. J.Y. performed cryo-EM data process. Y.J., J.Z. helped cryo-EM sample preparation. P.F. helped EM data analysis. J.Y., G.Y. and F.Y. built and refined the atomic model. All of the authors discussed the results. G.Y. wrote the manuscript.

DECLARATION OF INTERESTS

The authors declare no competing interests.

DATA AVAILABILITY

The cryo-EM maps of *At*HAK5, *At*HAK5$_{D152A}$ and the *Zm*HAK4 have been deposited in the Electron Microscopy Data Bank (EMDB) with the accession code EMD-68742, EMD-68736, and EMD-68733. The atomic coordinates for the corresponding model have been deposited in the Protein Data Bank (PDB) under the accession code 22WW, 22WQ, and 22WN, respectively.

DECLARATION OF GENERATIVE AI AND AI-ASSISTED TECHNOLOGIES IN THE WRITING PROCESS

During the preparation of this work, the authors used Gemini and ChatGPT in order to polish the English, making the final manuscript more concise. After using this tool/service, the authors carefully reviewed and edited the wording as needed and take full responsibility for the content of the published article.

REFERENCES

1 Maathuis, F. (1999). K+Nutrition and Na+Toxicity: The Basis of Cellular K+/Na+Ratios. Annals of Botany *84*, 123-133.

2 Mostofa, M.G., Rahman, M.M., Ghosh, T.K., Kabir, A.H., Abdelrahman, M., Rahman Khan, M.A., Mochida, K., and Tran, L.P. (2022). Potassium in plant physiological adaptation to abiotic stresses. Plant Physiol Biochem *186*, 279-289.

3 Nieves-Cordones, M., Al Shiblawi, F.R., and Sentenac, H. (2016). Roles and Transport of Sodium and Potassium in Plants. Met Ions Life Sci *16*, 291-324.

4 Johnson, R., Vishwakarma, K., Hossen, M.S., Kumar, V., Shackira, A.M., Puthur, J.T., Abdi, G., Sarraf, M., and Hasanuzzaman, M. (2022). Potassium in plants: Growth regulation, signaling, and environmental stress tolerance. Plant Physiol Biochem *172*, 56-69.

5 Wu, H., Zhang, X., Giraldo, J.P., and Shabala, S. (2018). It is not all about sodium: revealing tissue specificity and signalling roles of potassium in plant responses to salt stress. Plant and

Soil *431*, 1-17.

6 Yang, Y., and Guo, Y. (2018). Elucidating the molecular mechanisms mediating plant salt-stress responses. New Phytol *217*, 523-539.

7 Botella, M.A., Martinez, V., Pardines, J., and Cerdá, A. (1997). Salinity induced potassium deficiency in maize plants. Journal of Plant Physiology *150*, 200-205.

8 Adams, E., and Shin, R. (2014). Transport, signaling, and homeostasis of potassium and sodium in plants. J Integr Plant Biol *56*, 231-249.

9 Gierth, M., and Maser, P. (2007). Potassium transporters in plants--involvement in K+ acquisition, redistribution and homeostasis. FEBS Lett *581*, 2348-2356.

10 Basu, S., Kumar, A., Benazir, I., and Kumar, G. (2021). Reassessing the role of ion homeostasis for improving salinity tolerance in crop plants. Physiol Plant *171*, 502-519.

11 Lebaudy, A., Very, A.A., and Sentenac, H. (2007). K+ channel activity in plants: genes, regulations and functions. FEBS Lett *581*, 2357-2366.

12 Dreyer, I., and Uozumi, N. (2011). Potassium channels in plant cells. FEBS J *278*, 4293-4303.

13 Hamamoto, S., Horie, T., Hauser, F., Deinlein, U., Schroeder, J.I., and Uozumi, N. (2015). HKT transporters mediate salt stress resistance in plants: from structure and function to the field. Curr Opin Biotechnol *32*, 113-120.

14 Shi, H., Ishitani, M., Kim, C., and Zhu, J.K. (2000). The Arabidopsis thaliana salt tolerance gene SOS1 encodes a putative Na+/H+ antiporter. Proc Natl Acad Sci U S A *97*, 6896-6901.

15 Bassil, E., and Blumwald, E. (2014). The ins and outs of intracellular ion homeostasis: NHX-type cation/H(+) transporters. Curr Opin Plant Biol *22*, 1-6.

16 Li, W., Xu, G., Alli, A., and Yu, L. (2018). Plant HAK/KUP/KT K(+) transporters: Function and regulation. Semin Cell Dev Biol *74*, 133-141.

17 Hua, B.-G., Mercier, R.W., Leng, Q., and Berkowitz, G.A. (2003). Plants Do It Differently. A New Basis for Potassium/Sodium Selectivity in the Pore of an Ion Channel. Plant Physiology *132*, 1353-1361.

18 Gobert, A., Park, G., Amtmann, A., Sanders, D., and Maathuis, F.J. (2006). Arabidopsis thaliana cyclic nucleotide gated channel 3 forms a non-selective ion transporter involved in germination and cation transport. J Exp Bot *57*, 791-800.

19 Lau, A.M., Bordin, N., Kandathil, S.M., Sillitoe, I., Waman, V.P., Wells, J., Orengo, C.A., and Jones, D.T. (2024). Exploring structural diversity across the protein universe with The Encyclopedia of Domains. Science *386*, eadq4946.

20 Sillitoe, I., Bordin, N., Dawson, N., Waman, V.P., Ashford, P., Scholes, H.M., Pang, C.S.M., Woodridge, L., Rauer, C., Sen, N.*, et al.* (2021). CATH: increased structural coverage of functional space. Nucleic Acids Res *49*, D266-D273.

21 Ahmad, S., Jose da Costa Gonzales, L., Bowler-Barnett, E.H., Rice, D.L., Kim, M., Wijerathne, S., Luciani, A., Kandasaamy, S., Luo, J., Watkins, X.*, et al.* (2025). The UniProt website API: facilitating programmatic access to protein knowledge. Nucleic Acids Res *53*, W547-W553.

22 Wang, J., Luo, Y., Ye, F., Ding, Z.J., Zheng, S.J., Qiao, S., Wang, Y., Guo, J., Yang, W., and Su, N. (2024). Structures and ion transport mechanisms of plant high-affinity potassium transporters. Mol Plant *17*, 409-422.

23 Wang, X., Shen, X., Qu, Y., Zhang, H., Wang, C., Yang, F., and Shen, H. (2024). Structural insights into ion selectivity and transport mechanisms of Oryza sativa HKT2;1 and HKT2;2/1 transporters. Nat Plants *10*, 633-644.

24 Gao, R., Jia, Y., Xu, X., Fu, P., Zhou, J., and Yang, G. (2024). Structural insights into the Oryza sativa cation transporters HKTs in salt tolerance. J Integr Plant Biol *66*, 700-708.

25 Lu, Y., Yu, M., Jia, Y., Yang, F., Zhang, Y., Xu, X., Li, X., Yang, F., Lei, J., Wang, Y.*, et al.* (2022). Structural basis for the activity regulation of a potassium channel AKT1 from Arabidopsis. Nat Commun *13*, 5682.

26 Zhang, Y., Zhou, J., Ni, X., Wang, Q., Jia, Y., Xu, X., Wu, H., Fu, P., Wen, H., Guo, Y.*, et al.* (2023). Structural basis for the activity regulation of Salt Overly Sensitive 1 in Arabidopsis salt tolerance. Nat Plants *9*, 1915-1923.

27 Wang, Y., Pan, C., Chen, Q., Xie, Q., Gao, Y., He, L., Li, Y., Dong, Y., Jiang, X., and Zhao, Y. (2023). Architecture and autoinhibitory mechanism of the plasma membrane Na(+)/H(+) antiporter SOS1 in Arabidopsis. Nat Commun *14*, 4487.

28 Zhang, X.Y., Tang, L.H., Nie, J.W., Zhang, C.R., Han, X., Li, Q.Y., Qin, L., Wang, M.H., Huang, X., Yu, F.*, et al.* (2023). Structure and activation mechanism of the rice Salt Overly Sensitive 1 (SOS1) Na(+)/H(+) antiporter. Nat Plants *9*, 1924-1936.

29 Wang, J., Du, B.Y., Zhang, X., Qu, X., Yang, Y., Yang, Z., Wang, Y.F., and Zhang, P. (2025). Cryo-EM structures of Arabidopsis CNGC1 and CNGC5 reveal molecular mechanisms underlying gating and calcium selectivity. Nat Plants *11*, 632-642.

30 Xu, X., Wang, Q., Sun, T., Gao, H., Gu, R., Yang, J., Zhou, J., Fu, P., Wen, H., and Yang, G. (2025). Structural basis for the activity regulation of Medicago calcium channel CNGC15. Cell Discov *11*, 63.

31 Vieira-Pires, R.S., Szollosi, A., and Morais-Cabral, J.H. (2013). The structure of the KtrAB potassium transporter. Nature *496*, 323-328.

32 Chiang, W.T., Chang, Y.K., Hui, W.H., Chang, S.W., Liao, C.Y., Chang, Y.C., Chen, C.J., Wang, W.C., Lai, C.C., Wang, C.H.*, et al.* (2024). Structural basis and synergism of ATP and Na(+) activation in bacterial K(+) uptake system KtrAB. Nat Commun *15*, 3850.

33 Cao, Y., Pan, Y., Huang, H., Jin, X., Levin, E.J., Kloss, B., and Zhou, M. (2013). Gating of the TrkH ion channel by its associated RCK protein TrkA. Nature *496*, 317-322.

34 Zhang, H., Pan, Y., Hu, L., Hudson, M.A., Hofstetter, K.S., Xu, Z., Rong, M., Wang, Z., Prasad, B.V.V., Lockless, S.W.*, et al.* (2020). TrkA undergoes a tetramer-to-dimer conversion to open TrkH which enables changes in membrane potential. Nat Commun *11*, 547.

35 van Kempen, M., Kim, S.S., Tumescheit, C., Mirdita, M., Lee, J., Gilchrist, C.L.M., Soding, J., and Steinegger, M. (2024). Fast and accurate protein structure search with Foldseek. Nat Biotechnol *42*, 243-246.

36 Holm, L., Laiho, A., Toronen, P., and Salgado, M. (2023). DALI shines a light on remote homologs: One hundred discoveries. Protein Sci *32*, e4519.

37 Passaro, S., Corso, G., Wohlwend, J., Reveiz, M., Thaler, S., Somnath, V.R., Getz, N., Portnoi, T., Roy, J., Stark, H.*, et al.* (2025). Boltz-2: Towards Accurate and Efficient Binding Affinity Prediction. bioRxiv.

38 Rubio, F., Nieves-Cordones, M., Aleman, F., and Martinez, V. (2008). Relative contribution of AtHAK5 and AtAKT1 to K+ uptake in the high-affinity range of concentrations. Physiol Plant *134*, 598-608.

39 Qi, Z., Hampton, C.R., Shin, R., Barkla, B.J., White, P.J., and Schachtman, D.P. (2008). The high affinity K+transporter AtHAK5 plays a physiological rolein plantaat very low K+concentrations and provides a caesium uptake pathway inArabidopsis. Journal of Experimental Botany *59*, 595-607.

40 Abramson, J., Adler, J., Dunger, J., Evans, R., Green, T., Pritzel, A., Ronneberger, O., Willmore, L., Ballard, A.J., Bambrick, J.*, et al.* (2024). Accurate structure prediction of biomolecular interactions with AlphaFold 3. Nature *630*, 493-500.

41 Sousa, M.C., and McKay, D.B. (2001). Structure of the universal stress protein of Haemophilus influenzae. Structure *9*, 1135-1141.

42 Fuss, M.F., Wieferig, J.P., Corey, R.A., Hellmich, Y., Tascon, I., Sousa, J.S., Stansfeld, P.J., Vonck, J., and Hanelt, I. (2023). Cyclic di-AMP traps proton-coupled K(+) transporters of the KUP family in an inward-occluded conformation. Nat Commun *14*, 3683.

43 Maierhofer, T., Scherzer, S., Carpaneto, A., Muller, T.D., Pardo, J.M., Hanelt, I., Geiger, D., and Hedrich, R. (2024). Arabidopsis HAK5 under low K(+) availability operates as PMF powered high-affinity K(+) transporter. Nat Commun *15*, 8558.

44 Tascon, I., Sousa, J.S., Corey, R.A., Mills, D.J., Griwatz, D., Aumuller, N., Mikusevic, V., Stansfeld, P.J., Vonck, J., and Hanelt, I. (2020). Structural basis of proton-coupled potassium transport in the KUP family. Nat Commun *11*, 626.

45 Zhang, M., Liang, X., Wang, L., Cao, Y., Song, W., Shi, J., Lai, J., and Jiang, C. (2019). A HAK family Na(+) transporter confers natural variation of salt tolerance in maize. Nat Plants

5, 1297-1308.

46 Schweikhard, E.S., Kuhlmann, S.I., Kunte, H.J., Grammann, K., and Ziegler, C.M. (2010). Structure and function of the universal stress protein TeaD and its role in regulating the ectoine transporter TeaABC of Halomonas elongata DSM 2581(T). Biochemistry *49*, 2194-2204.

47 Fan, M., Zhang, J., Lee, C.L., Zhang, J., and Feng, L. (2023). Structure and thiazide inhibition mechanism of the human Na-Cl cotransporter. Nature *614*, 788-793.

48 Chi, G., Ebenhoch, R., Man, H., Tang, H., Tremblay, L.E., Reggiano, G., Qiu, X., Bohstedt, T., Liko, I., Almeida, F.G.*, et al.* (2021). Phospho-regulation, nucleotide binding and ion access control in potassium-chloride cotransporters. EMBO J *40*, e107294.

49 Zhao, Y., Vidossich, P., Forbush, B., Ma, J., Rinehart, J., De Vivo, M., and Cao, E. (2025). Structural basis for human NKCC1 inhibition by loop diuretic drugs. EMBO J *44*, 1540-1562.

50 Wan, Y., Guo, S., Zhen, W., Xu, L., Chen, X., Liu, F., Shen, Y., Liu, S., Hu, L., Wang, X.*, et al.* (2024). Structural basis of adenine nucleotides regulation and neurodegenerative pathology in ClC-3 exchanger. Nat Commun *15*, 6654.

51 Yang, Z., Zhang, X., Ye, S., Zheng, J., Huang, X., Yu, F., Chen, Z., Cai, S., and Zhang, P. (2023). Molecular mechanism underlying regulation of Arabidopsis CLCa transporter by nucleotides and phospholipids. Nat Commun *14*, 4879.

52 Rodenas, R., Ragel, P., Nieves-Cordones, M., Martinez-Martinez, A., Amo, J., Lara, A., Martinez, V., Quintero, F.J., Pardo, J.M., and Rubio, F. (2021). Insights into the mechanisms of transport and regulation of the arabidopsis high-affinity K+ transporter HAK51. Plant Physiol *185*, 1860-1874.

53 Ragel, P., Ródenas, R., García-Martín, E., Andrés, Z., Villalta, I., Nieves-Cordones, M., Rivero, R.M., Martínez, V., Pardo, J.M., Quintero, F.J.*, et al.* (2015). CIPK23 regulates HAK5-mediated high-affinity K+ uptake in Arabidopsis roots. Plant Physiology.

54 Emsley, P., and Cowtan, K. (2004). Coot: model-building tools for molecular graphics. Acta Crystallographica Section D *60*, 2126-2132.

55 Adams, P.D., Grosse-Kunstleve, R.W., Hung, L.-W., Ioerger, T.R., McCoy, A.J., Moriarty, N.W., Read, R.J., Sacchettini, J.C., Sauter, N.K., and Terwilliger, T.C. (2002). PHENIX: building new software for automated crystallographic structure determination. Acta Crystallographica Section D *58*, 1948-1954.

56 Delano, W.L. (2002). The PyMOL Molecular Graphics System.

57 Pettersen, E.F., Goddard, T.D., Huang, C.C., Couch, G.S., Greenblatt, D.M., Meng, E.C., and Ferrin, T.E. (2004). UCSF Chimera—A visualization system for exploratory research and analysis. Journal of Computational Chemistry *25*.

58 Banuelos, M.A., Klein, R.D., Alexander-Bowman, S.J., and Rodriguez-Navarro, A. (1995). A potassium transporter of the yeast Schwanniomyces occidentalis homologous to the Kup system of Escherichia coli has a high concentrative capacity. EMBO J *14*, 3021-3027.

59 Punjani, A., Rubinstein, J.L., Fleet, D.J., and Brubaker, M.A. (2017). cryoSPARC: algorithms for rapid unsupervised cryo-EM structure determination. Nat Methods *14*, 290-296.

60 Ashkenazy, H., Abadi, S., Martz, E., Chay, O., Mayrose, I., Pupko, T., and Ben-Tal, N. (2016). ConSurf 2016: an improved methodology to estimate and visualize evolutionary conservation in macromolecules. Nucleic Acids Res *44*, W344-350.

61 Pravda, L., Sehnal, D., Tousek, D., Navratilova, V., Bazgier, V., Berka, K., Svobodova Varekova, R., Koca, J., and Otyepka, M. (2018). MOLEonline: a web-based tool for analyzing channels, tunnels and pores (2018 update). Nucleic Acids Res *46*, W368-W373.

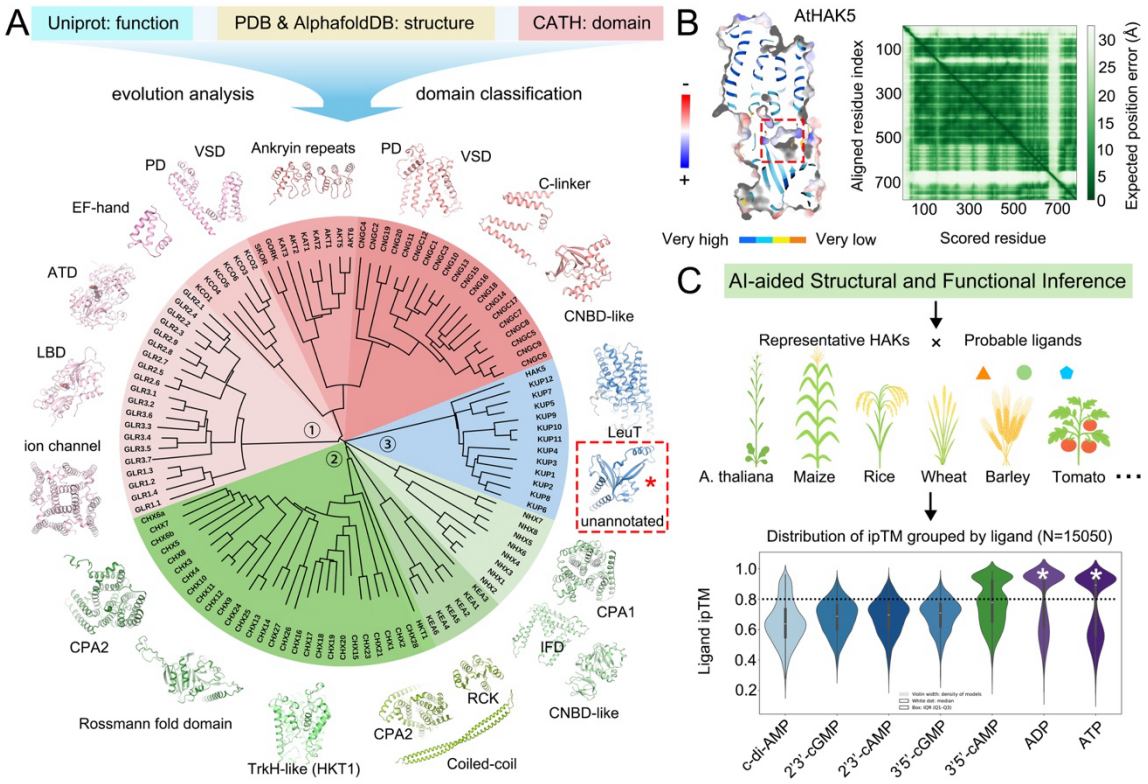

Figure 1. Domain clustering and AI-guided structural-functional prediction.

(A) Structural and domain clustering of *Arabidopsis thaliana* Na^+ and K^+ transport proteins based on UniProt[21], PDB, AlphaFoldDB[40], and CATH databases[20].

(B) AlphaFold3[40]-predicted structure of *At*HAK5, highlighting a highly charged cavity within the C-terminal cytoplasmic domain (CPD).

(C) Boltz2-driven ligand docking screen [37]across diverse HAK orthologs. ADP and ATP yielded the highest confidence ipTM scores among a library of nucleotide derivatives.

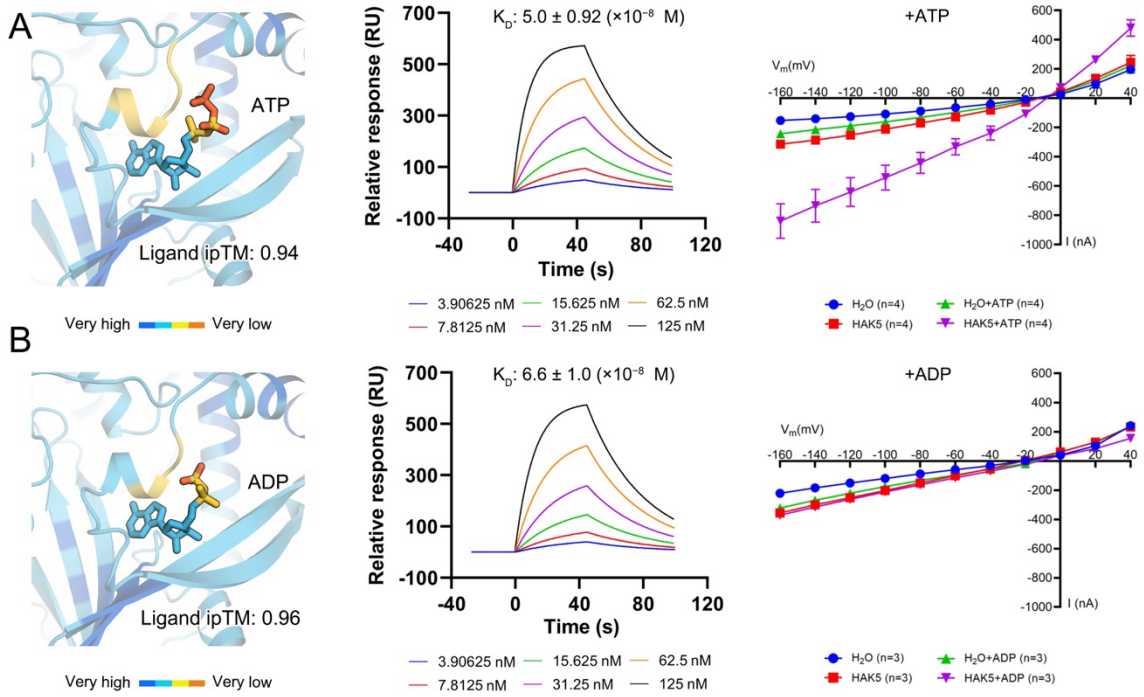

Figure 2. Validation of ATP/ADP binding and functional modulation of *At*HAK5.

(A, B) AlphaFold3[40]-predicted binding modes of ATP (top) and ADP (bottom) in the *At*HAK5 CPD, integrated with experimental validation. SPR sensorgrams (left) depict the binding kinetics and equilibrium dissociation constants (K_D) of ATP and ADP. K_D values were calculated from global fits of at least three independent experiments (mean ± SD). TEVC recordings (right) from *Xenopus* oocytes demonstrate the regulatory effects of ATP and ADP on K^+ currents. I-V curves represent steady-state peak currents (mean ± SEM).

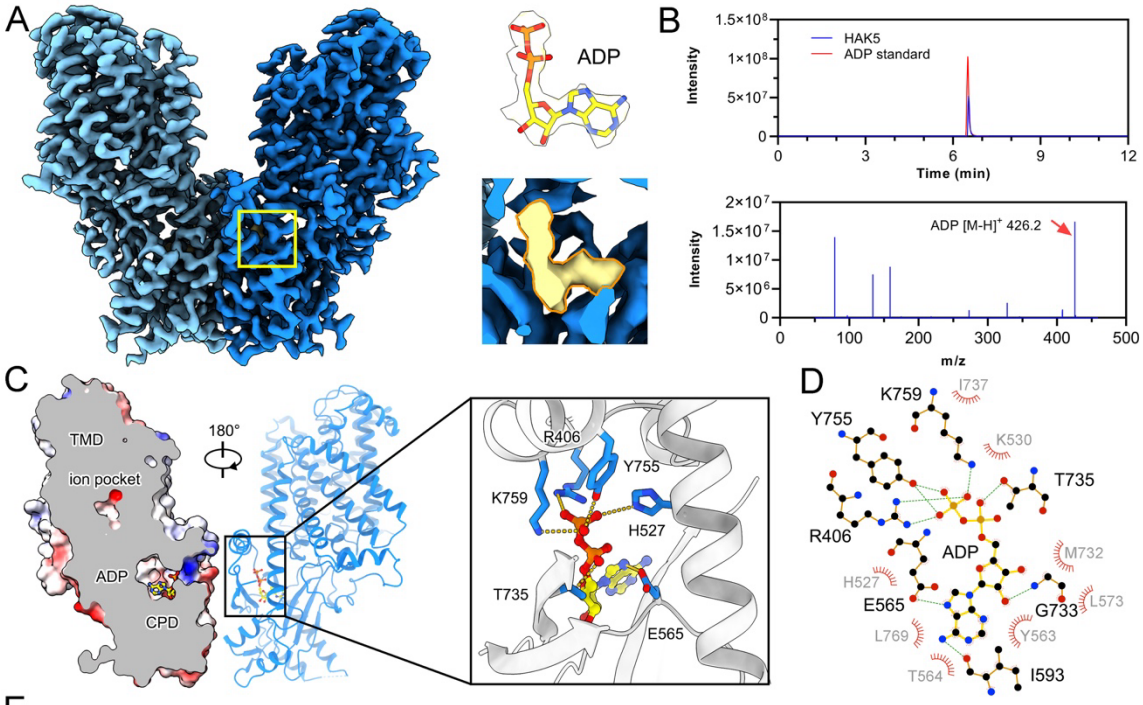

Figure 3. CryoEM structure of AtHAK5 reveals an endogenous bounded ADP.

(A) Cryo-EM density map of *At*HAK5 showing non-protein density in the CPD pocket that unambiguously accommodates ADP.

(B) Identification of the endogenous ligand as ADP via mass spectrometry. Retention times and fragmentation patterns of the *At*HAK5 sample match those of an ADP standard.

(C) Overall architecture and detailed interaction network of the ADP-binding pocket. ADP and its interacting residues are shown in sticks. Hydrogen bonds and salt bridges are shown by gold dashed lines.

(D) Schematic representation of ADP binding as shown by Ligplot^{+}. Hydrogen bonds and salt bridges are shown by dashed lines.

(E) Yeast complementation assay assessing the K^{+} transport activity of ADP-coordinating residue variants. Data are representative of n=3 independent experiments. EV, empty vector.

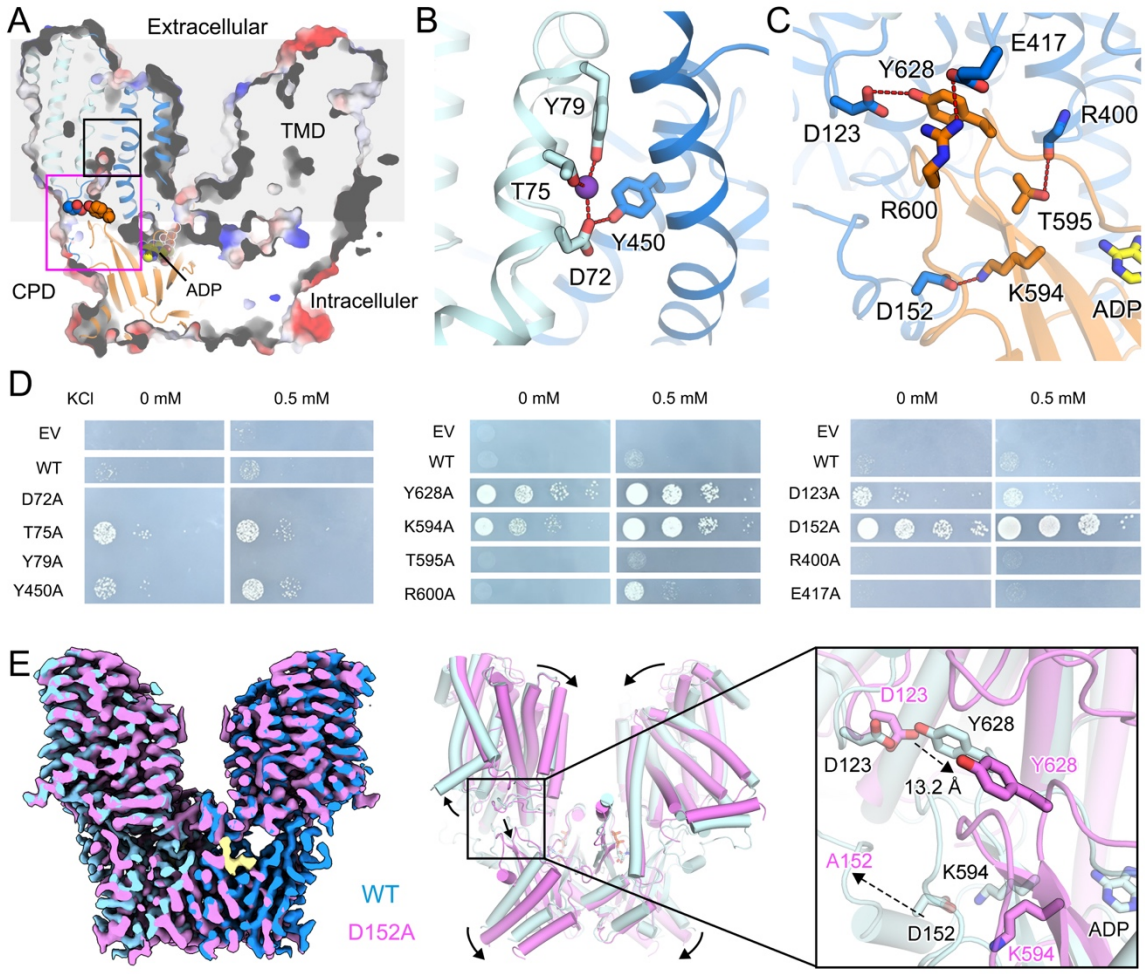

Figure 4. CPD rearrangement and ADP release underlie *At*HAK5 activation.

(A) Electrostatic surface representation of the K^+ transport pathway in ADP-bound *At*HAK5. Rectangles indicate the K^+ coordination cavity (black; detailed in B) and the TMD–CPD autoinhibitory interface (magenta; detailed in C).

(B, C) Molecular details of the K^+ binding site and the critical interactions stabilizing the TMD–CPD interface.

(D) Yeast growth analysis of alanine variants targeting the K^+ coordination site (left) and the TMD–CPD interface (middle/right). Disruption of the interface (e.g., D152A, K594A, Y628A) results in a dramatic gain-of-function phenotype.

(E) Structural overlay of *At*HAK5$_{WT}$ and the *At*HAK5$_{D152A}$ mutant. ADP is released from

639 *At*HAK5$_{D152A}$. The CPD of *At*HAK5$_{D152A}$ undergoes a substantial downward translocation,

640 dismantling the physical barrier in the transport pathway.

641

642

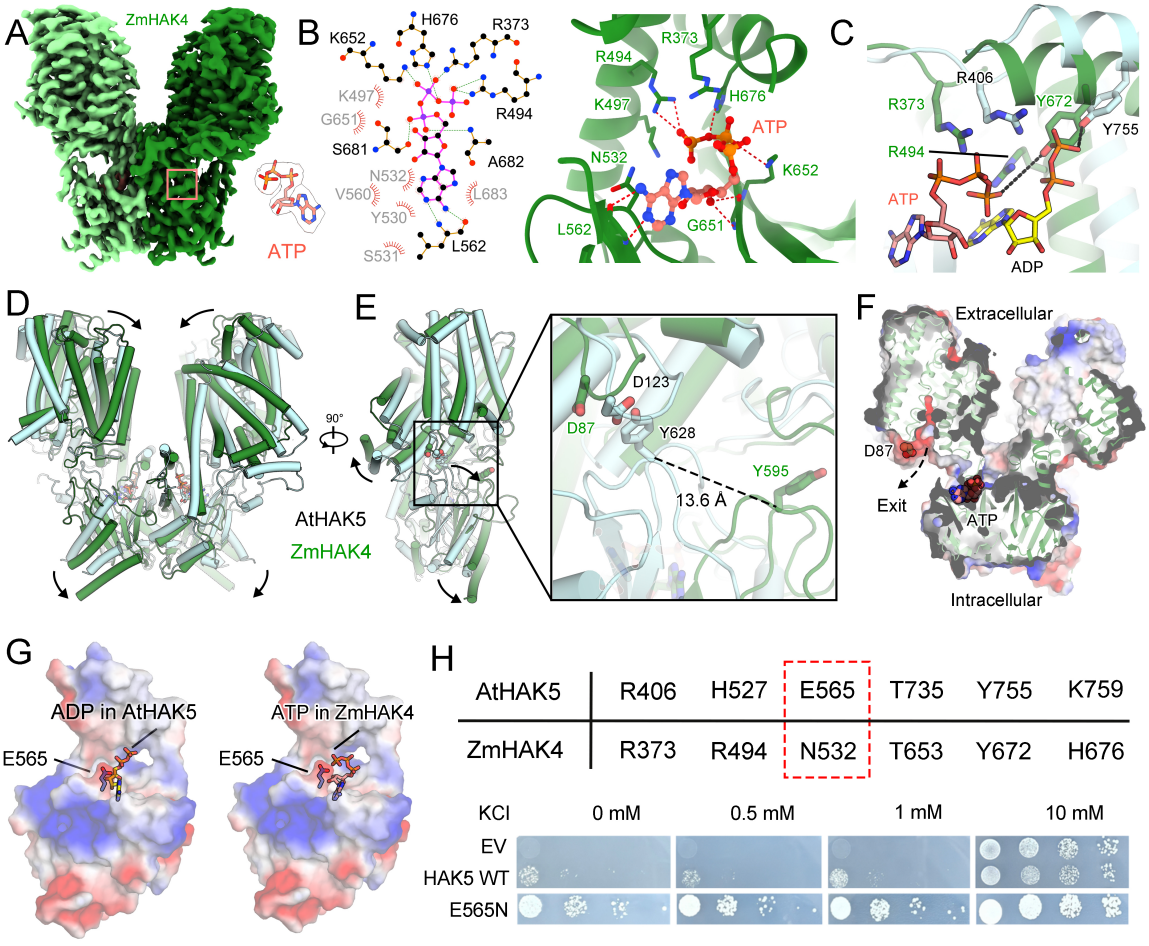

643

644 **Figure 5. The ATP-bound structure of *Zm*HAK4 recapitulates the activated state.**

645 **(A, B)** Cryo-EM density and atomic model of the *Zm*HAK4 CPD pocket occupied by ATP.

646 **(C-E)** Structural comparison between ADP-bound *At*HAK5 and ATP-bound *Zm*HAK4

647 exhibit large-scale displacement of the CPD.

648 **(F)** Surface representation of the unobstructed Na^+ pathway in *Zm*HAK4. The D87 in

649 *Zm*HAK4 is equivalent to the D123 in *At*HAK5.

650 **(G, H)** Electrostatic repulsion between Glu565 and the ATP triphosphate in *At*HAK5 limits

651 ATP occupancy. The E565N substitution (mimicking *Zm*HAK4) enhances K^+ transport.

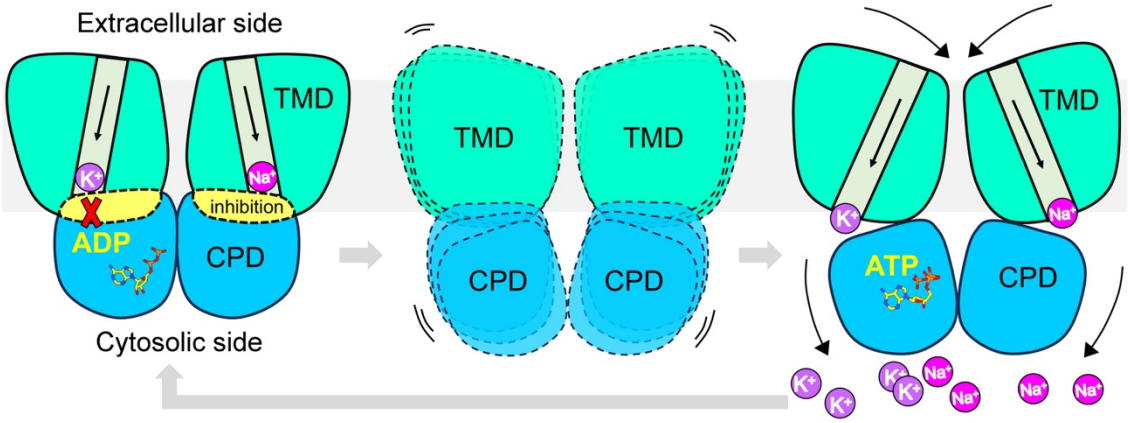

Figure 6. A plug-and-release model for the activity regulation of plant HAK transporters by ADP and ATP. In the ADP-bound state (left), the CPD inserts into the TMD to form a physical plug, locking the transporter in an autoinhibited conformation. Binding of ATP or phosphorylation triggers a large-scale conformational rearrangement where the CPD moves away from the TMD, switching the transport to an activated state. After activation, specific members like *At*HAK5 may lack the energetic stability to maintain the ATP-bound state, eventually returning to the ADP-inhibited ground state.

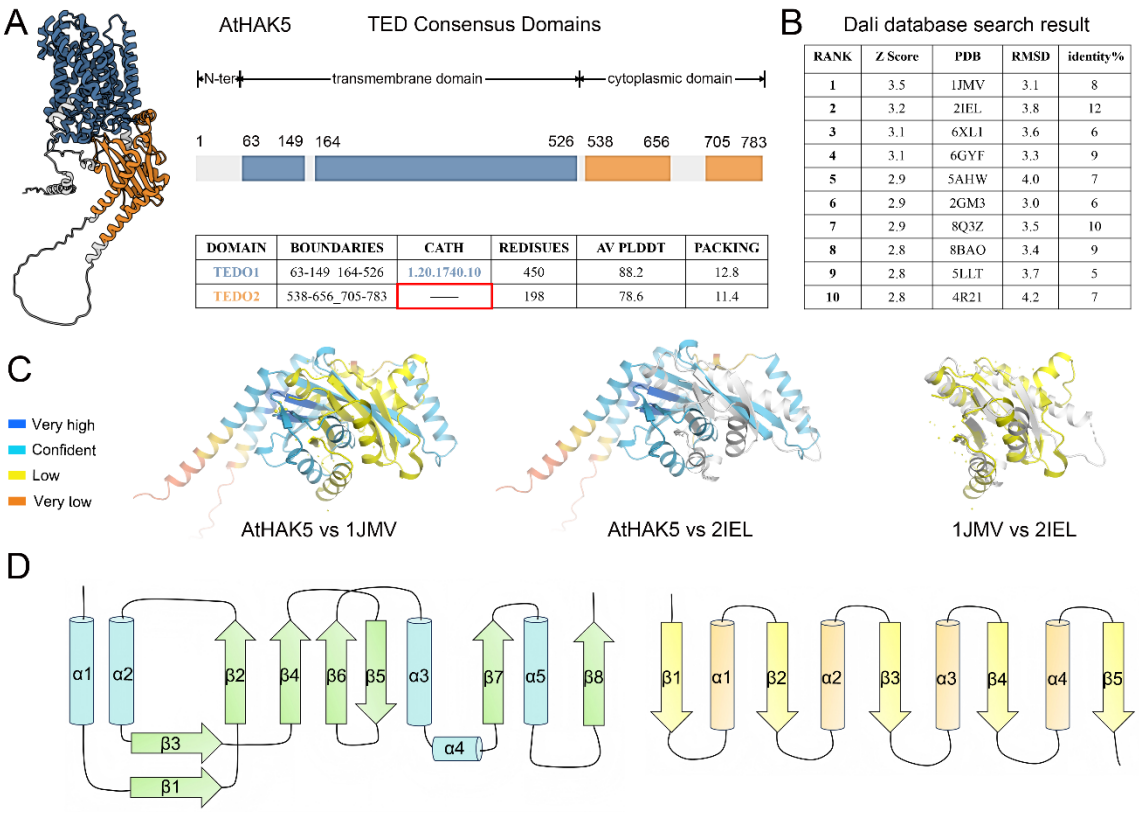

DOMAIN	BOUNDARIES	CATH	REDISUES	AV PLDDT	PACKING
TEDO1	63-149 164-526	1.20.1740.10	450	88.2	12.8
TEDO2	538-656_705-783	——	198	78.6	11.4

RANK	Z Score	PDB	RMSD	identity%
1	3.5	1JMV	3.1	8
2	3.2	2IEL	3.8	12
3	3.1	6XL1	3.6	6
4	3.1	6GYF	3.3	9
5	2.9	5AHW	4.0	7
6	2.9	2GM3	3.0	6
7	2.9	8Q3Z	3.5	10
8	2.8	8BAO	3.4	9
9	2.8	5LLT	3.7	5
10	2.8	4R21	4.2	7

Figure S1. AI-based discovery CPD of HAK transporters as a novel fold. (A) No CATH classification matches with the CPD of *At*HAK5 by TED database[19; 20]. The TED classifies the TMD of *At*HAK5 into a corresponding CATH but fails to assign any CATH category to the CPD. **(B)** Dali database search result of *At*HAK5 CPD structure predicted by AlphaFold3. 1JMV was the most identical structure with the highest Z score, but shares poor identity to the input. **(C)** Structural superimposition of *At*HAK5 CPD predicted by AlphaFold3, 1JMV and 2IEL searched by Dali. *At*HAK5 CPD shows completely distinct conformation with 1JMV and 2IEL. **(D)** Entirely different topology structure of *At*HAK5 CPD and 1JMV.

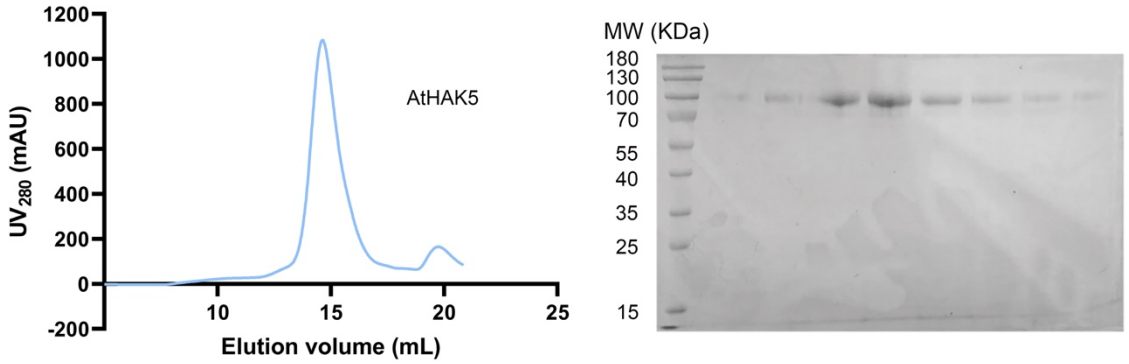

672

673 **Figure S2. Purification of *At*HAK5.** A representative gel-filtration chromatography of

674 *At*HAK5. The peak fractions were visualized on SDS–PAGE by Coomassie staining.

675 kDa, kilodaltons. MW, molecular weight marker.

676

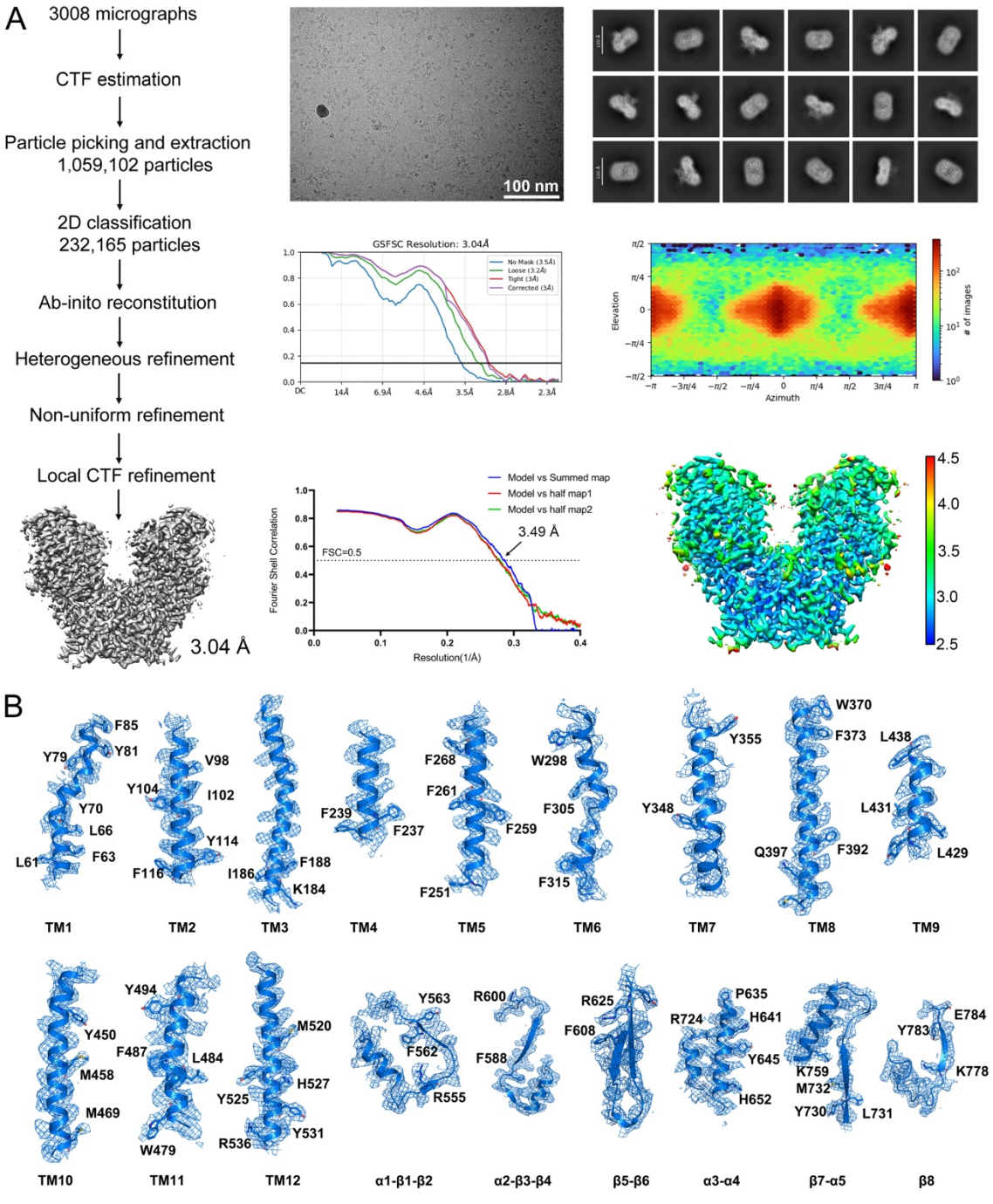

677

678 **Figure S3. Cryo-EM analysis of *At*HAK5.** Cryo-EM analysis of *At*HAK5. **(A)** Data

679 processing for *At*HAK5. The average resolution for the final reconstruction of *At*HAK5 is

680 estimated to be 3.04 Å. Details are described in the Methods. Representative micrograph

681 and 2D classification results are shown. Local resolution distribution of the final

682 reconstruction for *At*HAK5 is estimated by cryoSPARC[59]. **(B)** Representative EM

683 densities for *At*HAK5. The contour level of the EM density is 7σ.

684

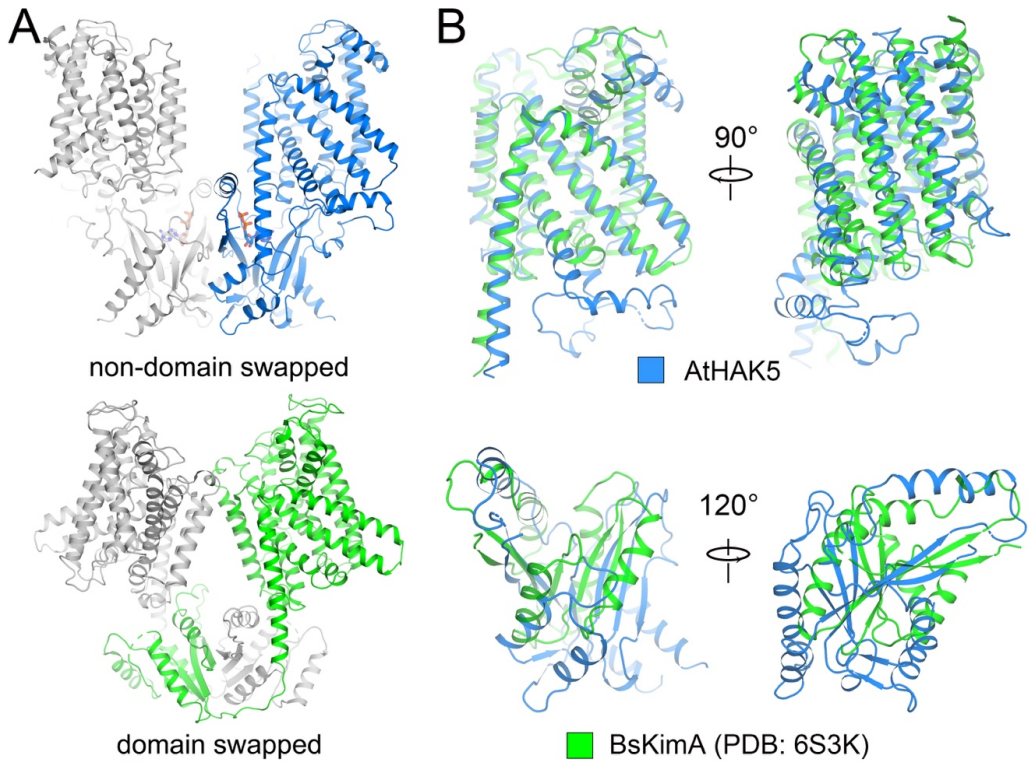

685

686 **Figure S4. Structural comparison of *At*HAK5 and *Bs*KimA. (A)** Overall structure of

687 *At*HAK5 and *Bs*KimA (PDB: 6S3K) [44]. *At*HAK5 has no domain swapped organization

688 like *Bs*KimA and only the CPD-CPD interactions stabilize the dimerization. **(B)** TMD

689 (upper panel) and CPD (lower panel) alignment of *At*HAK5 and *Bs*KimA. The TMD of

690 them share similar topologies and structures, while the CPD are obviously different.

691

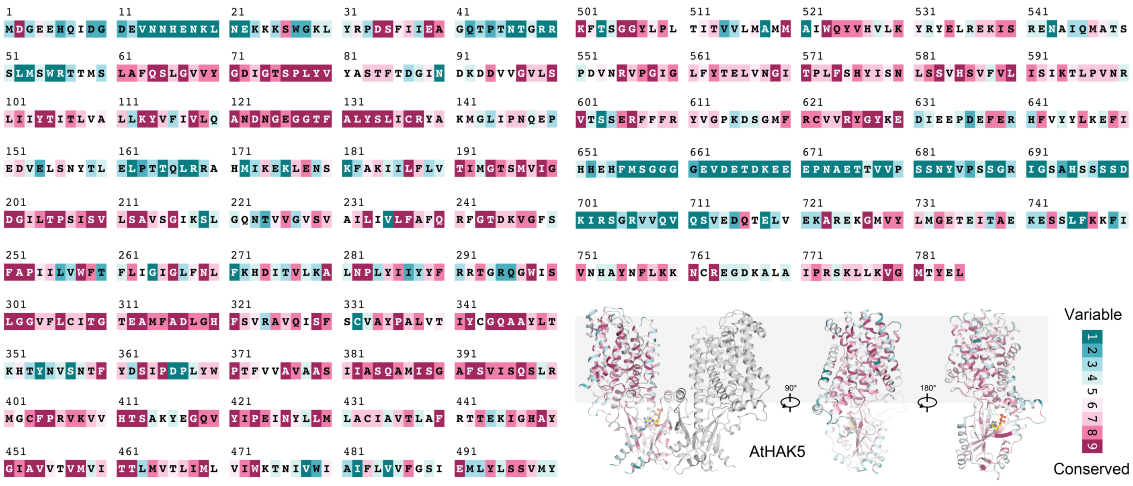

Figure S5. Sequence conservation onto the structure of *At*HAK5. The conservation map was generated across 150 automatically selected HAK family members using ConSurf[60].

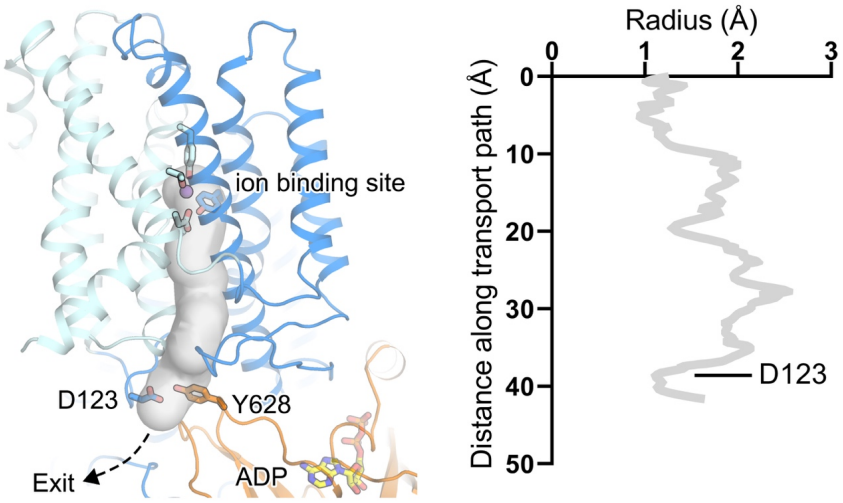

Figure S6. Ion accessible pathway of *At*HAK5. The ion transport pathway starts from K^+ coordination site and extends into the CPD of the ADP-bound *At*HAK5, both Asp123 and Tyr628 insert into the pathway and form an interaction to obstruct K^+ transport. The pore radius of *At*HAK5 was calculated by MOLE[61].

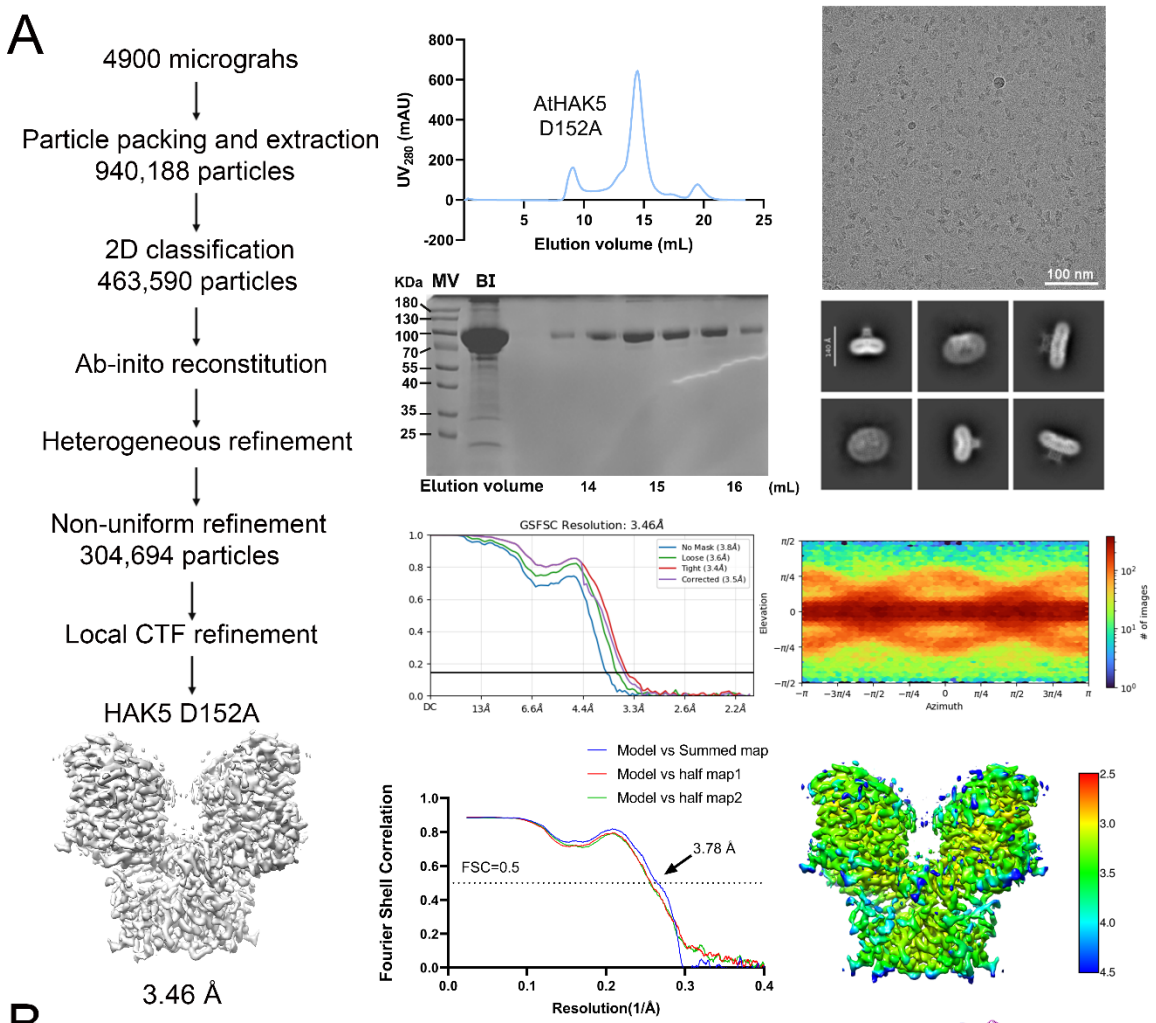

Figure S7. Cryo-EM analysis of *At*HAK5$_{D152A}$. **(A)** Protein purification and data processing for *At*HAK5$_{D152A}$. The average resolution for the final reconstruction of *At*HAK5$_{D152A}$ is estimated to be 3.46 Å. Details are described in the Methods. Representative gel-filtration chromatography, SDS-PAGE of peak fractions, representative micrograph and 2D classification results are shown. BI, before gel-filtration injection. Local resolution distribution of the final reconstruction for *At*HAK5$_{D152A}$ is estimated by cryoSPARC[59]. **(B)** Representative EM densities for *At*HAK5$_{D152A}$. The contour level of the EM density is 7σ.

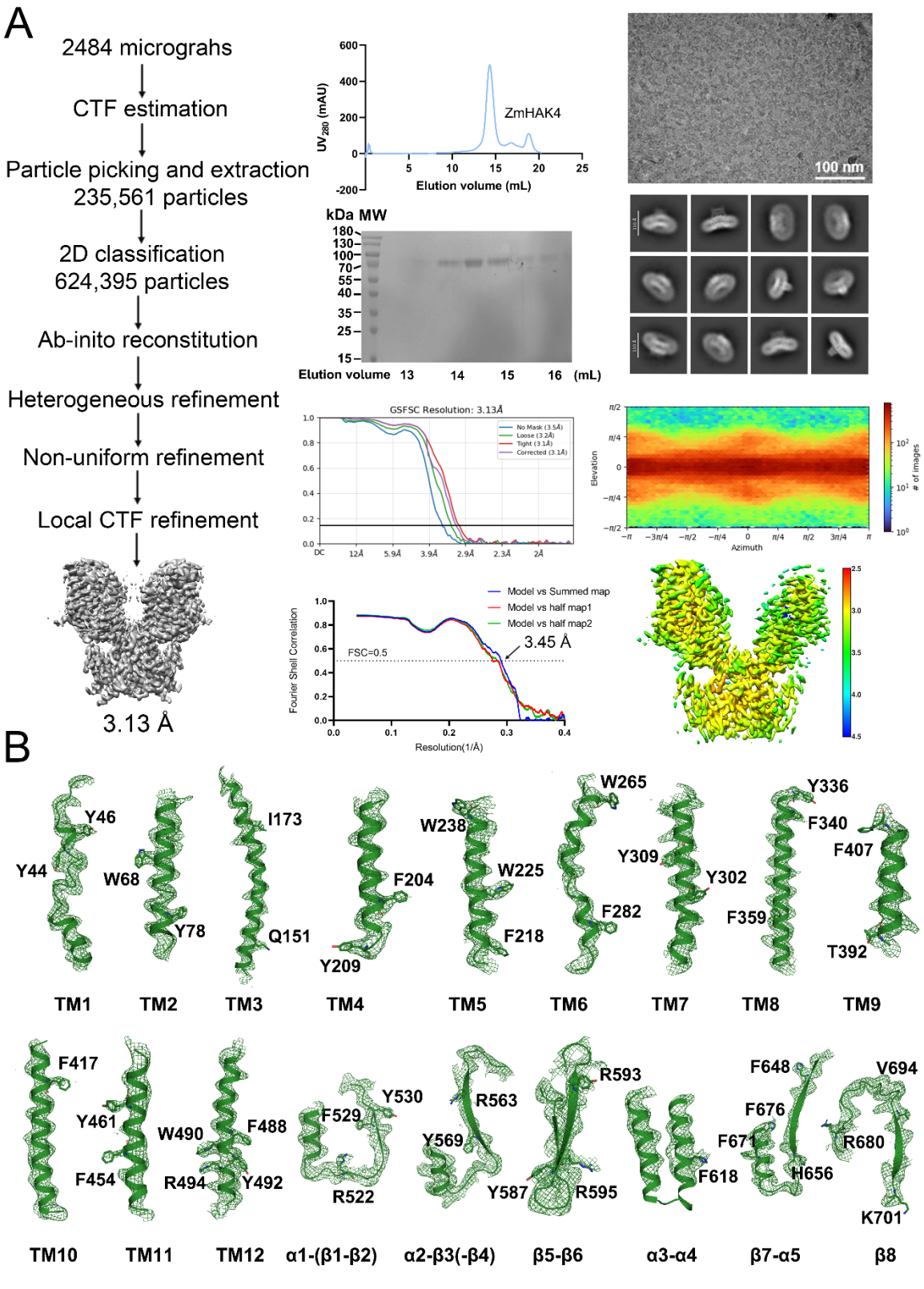

Figure S8. Cryo-EM analysis of *Zm*HAK4. (A) Protein purification and data processing for *Zm*HAK4. The average resolution for the final reconstruction of *Zm*HAK4 is estimated to be 3.13 Å. Details are described in the Methods. Representative gel-filtration chromatography, SDS-PAGE of peak fractions, micrograph and 2D classification results are shown. Local resolution distribution of the final reconstruction for *Zm*HAK4 is estimated by cryoSPARC[59]. **(B)** Representative EM densities for *Zm*HAK4. The contour level of the EM density is 7σ.

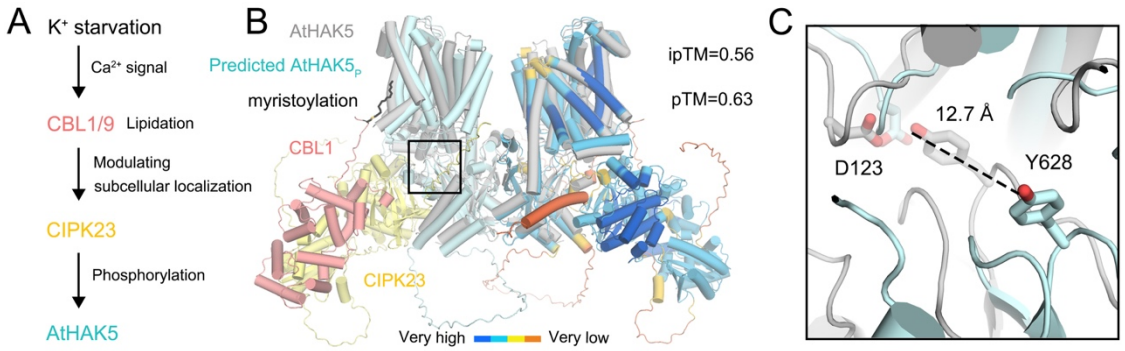

Figure S9. Phosphorylation of *At*HAK5 induces a superimposable switch to *At*HAK5$_{D152A}$. **(A)** Schematic model for phosphorylation-related activation of *At*HAK5. K^+ starvation causes Ca^{2+} signal, results in the calcineurin B-like protein 1 or 9 (CBL1/9) locating on plasma by lapidation to activate CBL-interacting serine/threonine-protein kinase 23 (CIPK23). The activated CIPK23 directly phosphorylates AtHAK5 N-terminal to enhance K^+ transport. **(B)** Structure model of *At*HAK5/CIPK23/CBL1 complex by AlphaFold3[40]. CIPK23 is modeled to touch and potentially disturb the key interaction on TMD-CPD interface as the complex structure drives a comparable conformational change to *At*HAK5$_{D152A}$ with the TMD keeping away from the CPD. **(C)** Conformational rearrangement of Tyr628 abrogates autoinhibitory in phosphorylation complex. The structural rearrangement of Tyr628 produces a 12.7 Å distance between Asp123 and Try628, abolishes the steric hindrance on the ion conduction pathway.

736 **Supplemental Table 1. Cryo-EM data collection, refinement and validation**.

Coordinates	22WW	22WQ	22WN
EMDB	EMD-68742	EMD-68736	EMD-68733
Data collection and processing	*At*HAK5	*At*HAK5$_{D152A}$	*Zm*HAK4
Voltage (kV)	300	300	300
Electron exposure (e–/Å^2)	50	50	50
Defocus range (μm)	-1.3 ~ -1.8	-1.3 ~ -1.8	-1.3 ~ -1.8
Pixel size (Å)	1.0825	1.032	0.8374
Symmetry imposed	C2	C2	C2
Map resolution (Å)	3.04	3.46	3.13
FSC threshold	0.143	0.143	0.143
Refinement			
Model composition			
Non-hydrogen atoms	10,810	10,460	10,288
Protein residues	1358	1324	1306
Ligands	4	0	2
B-factors (Å^2)			
Protein	60.50	187.03	84.41
Ligand	35.22	-	46.91
R.m.s. deviations			
Bond lengths (Å)	0.003	0.004	0.003
Bond angles (°)	0.529	0.830	0.598
Validation			
MolProbity score	1.82	2.36	2.05
Clashscore	6.69	12.98	7.85
Poor rotamers (%)	1.86	2.61	2.21
Ramachandran plot			
Favored (%)	96.37	93.67	94.74
Allowed (%)	3.63	6.10	5.18
Disallowed (%)	0	0.23	0.08

737